

Title Page

Bio-tribocorrosion mechanisms in orthopaedic devices: mapping the micro-abrasion-corrosion behaviour of a simulated CoCrMo hip replacement in calf serum solution

K. Sadiq^{a, b*}, M.M. Stack^a, R.A. Black^b

^a Department of Mechanical Engineering, University of Strathclyde, 75 Montrose St., Glasgow, G1 1XJ, UK

^b Department of Biomedical Engineering, University of Strathclyde, Wolfson Centre, 106 Rottenrow, Glasgow, G4 0NW, UK

*** Corresponding author**

K. Sadiq

Tel.: +44 141 574 5079

E-mail address: kamran.sadiq@strath.ac.uk (K. Sadiq)

Abstract

Load bearing implant prostheses such as orthopaedic hip and knee implants may be considered as tribocorrosion systems since the wear processes are a result of combined mechanical and chemical mechanisms. The long-term success of implant prostheses depends on a number of factors, including age, body weight and activity levels. Pre-clinical testing is therefore crucial in determining the long-term performance, safety and reliability of the implant *in-vivo*. In this study CoCrMo alloy and UHMWPE couple was tested in a physiological solution of foetal calf serum (FCS) in 0.9 wt. % NaCl to assess the underlying wear mechanisms as a result of applied load (0-5N) and applied potential (-600, -400, -200, 0 and +200 mV). The transitioning behaviours due to micro-abrasion and corrosion were studied; corresponding micro-abrasion-corrosion wear maps were constructed to indicate the mass loss transitions in scope of wastage, mechanisms of wear and synergies between abrasion-corrosion for simulated hip contact conditions.

Keywords

Bio-tribocorrosion

CoCrMo

Hip replacement

Calf serum

Tribocorrosion maps

Introduction

Wear mapping provides a useful approach for solving wear related problems of materials operating in a wide range of conditions [1, 2]. Such a tool in engineering enables a powerful means to describe wear mechanisms, interactions and transitions during the wear process. Mapping can enable the wear prediction and optimisation of specific material combinations for any given operating environment, Lim and Ashby demonstrated mapping of wear mechanisms as early as 1987 [3].

When tribological contacts operate in a corrosive environment, material degradation occurs due to both mechanical and chemical mechanisms. More recently it has been established that material mass loss is not simply a summation of the individual mechanical and chemical components i.e. tribocorrosion. In a tribocorrosion system there is an interaction between the wear components, which may result in accelerated material degradation [4]. Tribocorrosion is defined as an irreversible transformation of a material resulting from simultaneous physico-chemical and mechanical interactions occurring in a tribological contact [4].

The wear performance of biomedical implants from a tribocorrosion perspective remains a developing area [5]. Considering the prevalent high clinical failure rates observed in metal-on-metal hip replacement in recent times, and the associated adverse health risks [6], more durable implants are required. This can only be achieved by studying all factors that influence wear and wear rates. Buford and Goswami [7] showed the wear mechanisms in hip replacement are a function of the material type, contact stresses, lubricants and clearance, surface hardness and roughness, type of articulation due to motion, cycles, solution particle count and distribution, and oxidative wear. Furthermore it is clear from the wider literature that standardised pre-clinical hip simulator based-testing for total hip replacement has so far been unable to reliably predict or achieve realistic and clinically relevant wear rates [8, 9] with serious ramifications for patients, healthcare providers and orthopaedic manufacturers. There is a definite need to understand comprehensively the underlying wear mechanisms occurring in orthopaedic implant prostheses (e.g. Total Hip Replacement) as a tribocorrosion system [5, 6, 8]. Additionally, progress has been limited, and few reliable tribocorrosion wear maps specific to total hip replacement prostheses exist to date. Such maps may be a valuable tool for device manufacturers to predict long-term wear and subsequent implant performance and patient health outcomes.

Combined micro-scale abrasion and corrosion studies in the context of orthopaedic implants are still a relatively recent development. Micro-abrasion testing is the study of material wear due to the interaction of a third body in a two body sliding contact, usually in the form of small particles typically 10 μm or less [9]. Micro-abrasion wear for a wide range of materials and coatings, including biomaterials have been studied in recent years. Sun et al. studied the combined micro-abrasion and corrosion [10-12], more recently nano-abrasion-corrosion of cast CoCrMo [13]. They showed the varying effects of the interacting micro-abrasion and corrosion of CoCrMo in the presence of protein solution and different concentrations of particles. Variations of the testing solution compositions were shown to have a significant influence on the wear-corrosion mechanisms. The work has further demonstrated the presence of protein in solution gives rise to the formation of a surface film comprising metal-protein complexes that also influences the cathodic kinetics. In

related work elsewhere Wimmer et al. (2010) [14] studied specifically the formation and action of tribochemical reaction layers in metal-on-metal hip replacement. They found that the surface layers are frequently formed on the metal hip surfaces based on *in-vitro* and implant retrieval studies; the authors concluded that the layers are composed of nanocrystalline composites of metallic, ceramic and organic material generated by mechanical mixing. The stabilisation of such surface protein layers may act as a lubricant enabling lower wear rates.

Previous work by one of the current authors (M. M. Stack) has focused on mapping the micro-abrasion-corrosion behaviour of CoCrMo alloy in Ringer's solution [15]. The wear maps showed the transitioning micro-abrasion-corrosion wear losses, mechanisms, and synergisms for simulated hip contact. Similarly, the focus of this study was to characterise and map the micro-abrasion-corrosion performance of CoCrMo during simulated hip contact conditions in protein solution (Foetal Calf Serum 10 vol.% in NaCl), as a function of applied load and applied potential, with a view to mapping specific abrasion-corrosion transitions in the physiological range of loading conditions. In this study the transitioning micro-abrasion-corrosion mechanisms, wastage rates and synergistic behaviours were identified and mapped for CoCrMo alloy in protein solution.

2. Materials & Methods

2.1. Experimental overview

A micro-scale abrasion apparatus (also known as ball cratering) was selected for simulating the hip conditions for the following reasons:

- Small-scale tribological test
- Rapid and low-cost localised abrasion on small samples
- Robust and repeatable
- Integration of electrochemical cell
- Understanding the abrasion-corrosion wear mechanisms in biological solution
- Understanding the passivation behaviour during micro-abrasion-corrosion

2.1.1. CoCrMo specimens

The CoCrMo (ASTM F1537) specimens were provided by Rush University Medical Centre, USA and arrived pre-machined from rods of low-carbon (LC) CoCrMo wrought alloy. The specimens were supplied as disks 29mm in diameter and 4mm in thickness. The chemical composition and material properties are shown in Table 1 and Table 2. Prior to testing the surfaces were ground and polished to a mirror finish using conventional metallographic techniques ($R_a = 0.002 \pm 0.01 \mu\text{m}$), the surface roughness was measured using an MFP-3D Atomic Force Microscope (Asylum Research, CA).

Table 1: Chemical composition of CoCrMo

Element	Chemical Composition (wt. %)
Co	Bal.
Cr	27.56
Mo	5.70
Mn	0.60
Si	0.38
C	0.03
Al	<0.02

Table 2: Material properties

Material	Source	Density (kg/m ³)	Vickers Hardness
Wrought CoCrMo alloy	ALLVAC (USA)	8300	390 <i>max</i>
UHMWPE	K-mac Plastics (USA)	931-935	541

2.1.2. Protein test solution

The test solution used for the micro-abrasion-corrosion testing consisted of 0.9 wt. % sodium chloride (NaCl) supplied by Sigma-Aldrich (UK) and 10 vol. % foetal calf serum (FCS) supplied by Biosera (UK), the solution had a pH value of 7.3. The solution was selected because it is a simple simulated biological fluid and contains a similar level of chloride to that in human body fluids, the additional FCS was used to evaluate the effect of protein on the micro-abrasion-corrosion behaviour of the test specimen. The solution was prepared and refrigerated 1 day prior to testing.

2.2. Micro-abrasion-corrosion apparatus

Micro-abrasion testing was conducted on a commercially available apparatus, the TE-66 micro-abrasion tester (Phoenix Tribology, UK). The apparatus was modified to measure electrochemical activity and to control the applied potential during micro-abrasion using a Gill AC electrochemical interface (ACM Instruments, UK). Figure 1 shows a schematic diagram of the modified apparatus. For measuring the estimate corrosion rate, the test specimen (working electrode) and a Pt-Ti wire mesh (auxiliary electrode) were connected to the rig, to complete the three-electrode electrochemical setup a reference electrode (SCE) was connected by a capillary tube in contact with the test solution.

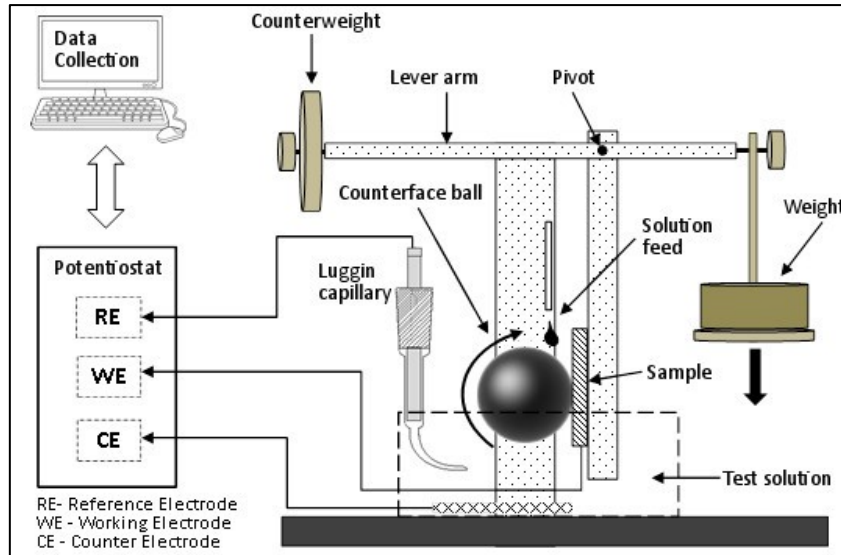


Figure 1: Micro-abrasion-corrosion test apparatus

The micro-abrasion rig consisted of a 25mm UHMWPE ball located between two coaxial shafts carried by support bearings, and one shaft was driven by a variable speed DC geared motor. An in-built batch counter measured the number of shaft revolutions during operation. The physiological test solution was delivered to the specimen-ball contact by a peristaltic pump head connected to the other end of the shaft. The test specimen was clamped onto a platform, which was fitted to the pivoted L-shaped arm, the arm was rotated around its pivot until the sample and ball made physical contact. The load was applied by adding dead weights to a cantilever arm. The test solution (0.9 wt.% NaCl and 10 vol.% FCS) was stored in a glass container and delivered to the specimen-ball by an integrated peristaltic pump. The solution was fed to a point closely above the specimen-ball contact point and collected in a waste tray underneath. Several tests could be conducted on a single test specimen by moving the arm, which holds the specimen in a horizontal direction.

On completion of testing, each test specimen was removed from the sample holder and the diameter of the resulting abrasion scar was measured with optical microscope (Zeiss ApoTome) using the Zeiss AxioVision software package. Further detailed micrographs were acquired using tungsten filament SEM (Hitachi S-3700) and AFM MFP-3D (Asylum Research, CA). Samples were rinsed in distilled water and allowed to air dry prior to imaging. Repeat tests were carried out at various applied loads and applied potentials. The wear volume was calculated using the standard technique for measuring wear scar of spherical geometry [9], i.e. it is assumed the shape of the crater is conformal to the shape of the ball. The wear volume (V) may then be calculated by measurement of the crater diameter (b) and R the ball radius (for $b \ll R$). Repeat tests ($n=3$) were carried out for various applied loads, the experimental error was estimated to be $\pm 9\%$. Figure 9 shows the experimental error for the resulting mass losses at 0 mV applied potential.

$$V \approx \frac{\pi b^4}{64R} \quad \text{For } b \ll R \quad (1)$$

2.3. Testing procedure

The effects of applied potential and applied load were varied to study the micro-abrasion-corrosion response under those conditions; Figure 2 provides a diagrammatic description of the complete testing procedure. The temperature of the test solution was kept at a room temperature of around 25°C and contained within a sterile glass container, from which the pump directly fed solution to the specimen-ball contact. Tests were carried out at various applied loads (0.5-5N) for duration of 30 minutes each, the ball rotated at a speed of 100 rpm for 3000 rev (235.50 m sliding distance). Polarisation sweeps were conducted at a sweep rate of 83.33 mV/min over the range -1.5V to +1.5V, measurements for increasing applied load were recorded. Potentiostatic tests were conducted also for increasing applied potential (-600, -400, -200, 0, +200 mV, SCE) and corrosion rates (K_c) estimated by the corresponding measured current densities at the various applied loads.

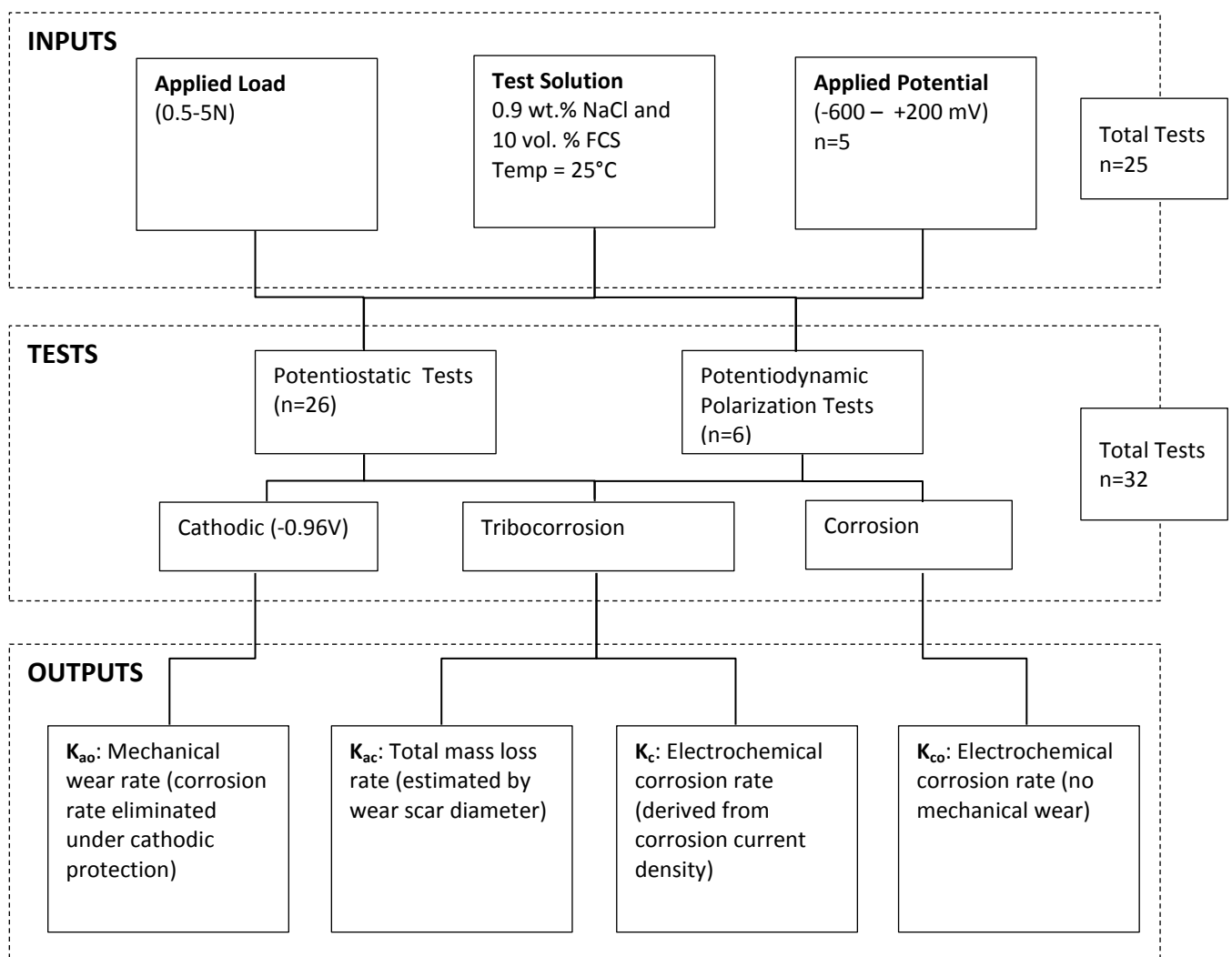
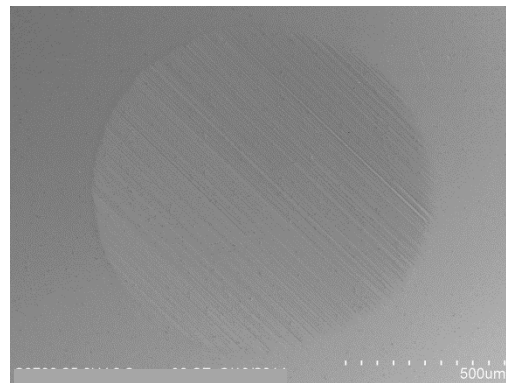


Figure 2: Micro-abrasion-corrosion testing procedure for CoCrMo alloy in physiological solution

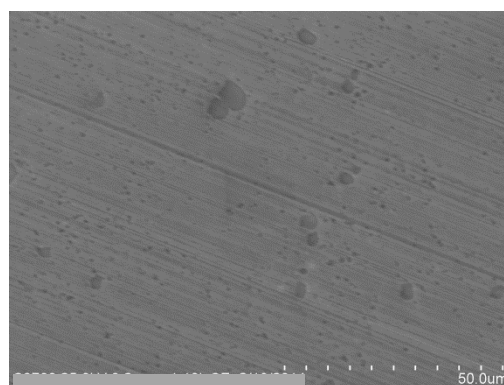
3. Results

3.1. Scar imaging

Images of the scars generated during testing were obtained using optical microscopy and SEM (Fig. 3a). The scar diameters at each applied load vs. applied potential (n=25) were measured in order to estimate the total mass loss of material as described in equation 1. The images showed clear and distinct parallel grooves in the direction of sliding visible within the crater, generally indicating a 2-body dominant abrasion regime across the range of tests conducted. There appears to be minimal indication of 3-body abrasion for the tests performed in protein solution; this may be due to the presence of protein acting as lubricant but it is not conclusive. It is important to highlight that during the testing no additional particles were added to the test solution for the scars shown. At a closer inspection using SEM (Fig. 3b), small particles are visible shown embedded on the surface of the wear grooves. It is not certain but the particles shown may have been responsible for the abrasion (due to micro-cutting or ploughing) and may be composed of a mixture of polyethylene, protein and metal from the alloy.



(a)



(b)

Figure 3: SEM scans showing wear scars for CoCrMo generated at an applied load of 5N during +200 mV applied potential: a) scar diameter; b) parallel grooves with embedded particles on crater surface. Image scales indicated on micrographs.

AFM scans (Fig. 4) further revealed clear indication of 2-body abrasion over the range of testing, small particles are embedded on the crater surface. It should also be noted however that the objective of scar imaging was mainly to determine the volumetric loss of material, more in-depth analysis of the wear patterns and surface composition will be the objective of further work.

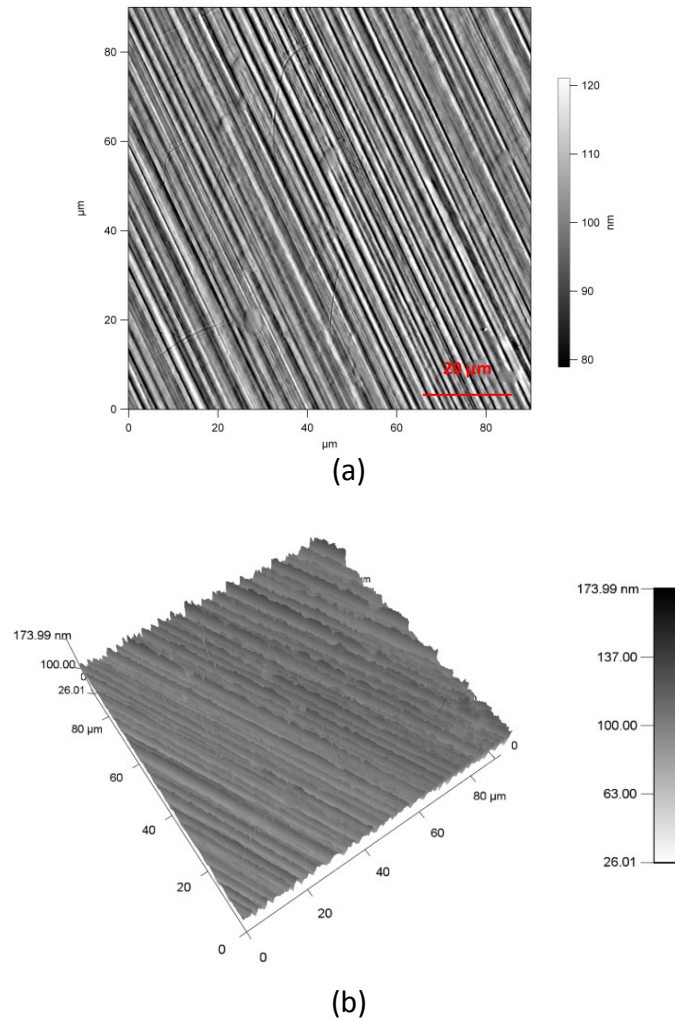
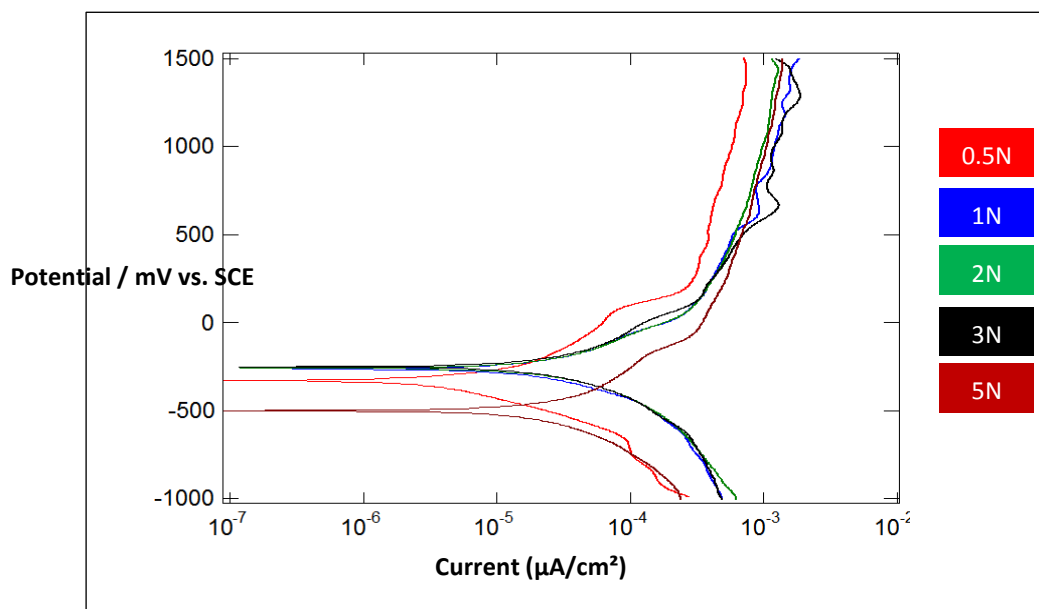


Figure 4: AFM scans of wear scar surface for an applied load of 5N vs. applied potential +200 mV: a) distinct parallel grooves across the surface indicating a 2-body abrasion regime, small particles appear to be embedded at the surface; b) 3D scan image for the scar surface indicates the depth of the abraded grooves. Height scale shown to the right.

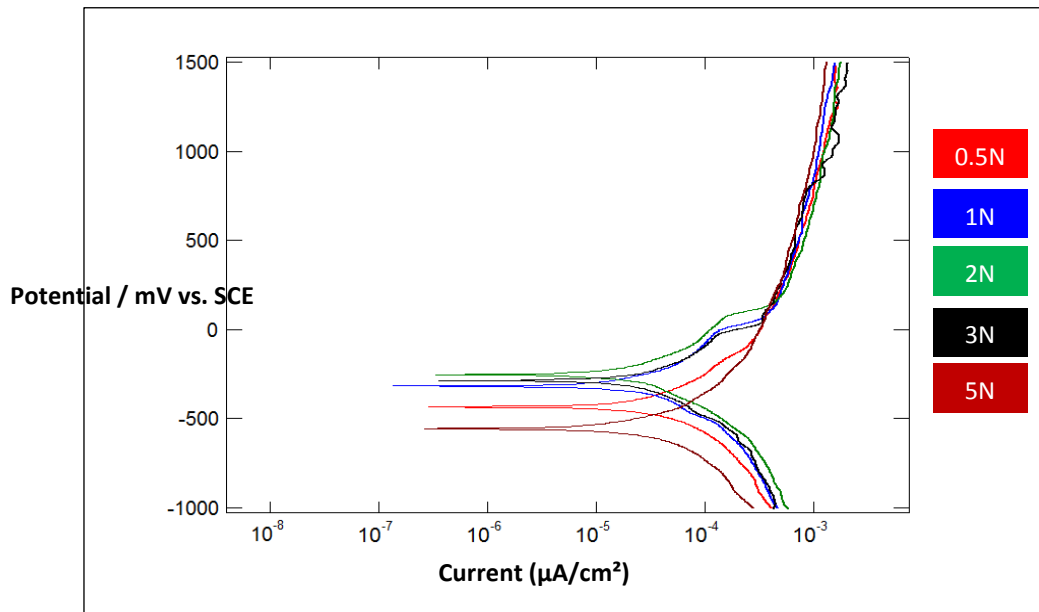
2.1. Polarisation sweep measurements

The effect of applied load and applied potential on the general electrochemical behavior was investigated with potentiodynamic polarisation sweeps. Curves recorded for increasing applied load ranging from 0.5N to 5N are shown in Fig. 5a. A shift in E_{corr} towards more anodic potentials and in increase of the current densities are clearly observed as the applied load is increased. This could indicate an enhanced wear behaviour which appears to act only for a limited range of applied load, at the maximum applied load (5N) there is a clear negative shift in E_{corr} and a lower i_{corr} indicating an enhanced passivation behaviour.

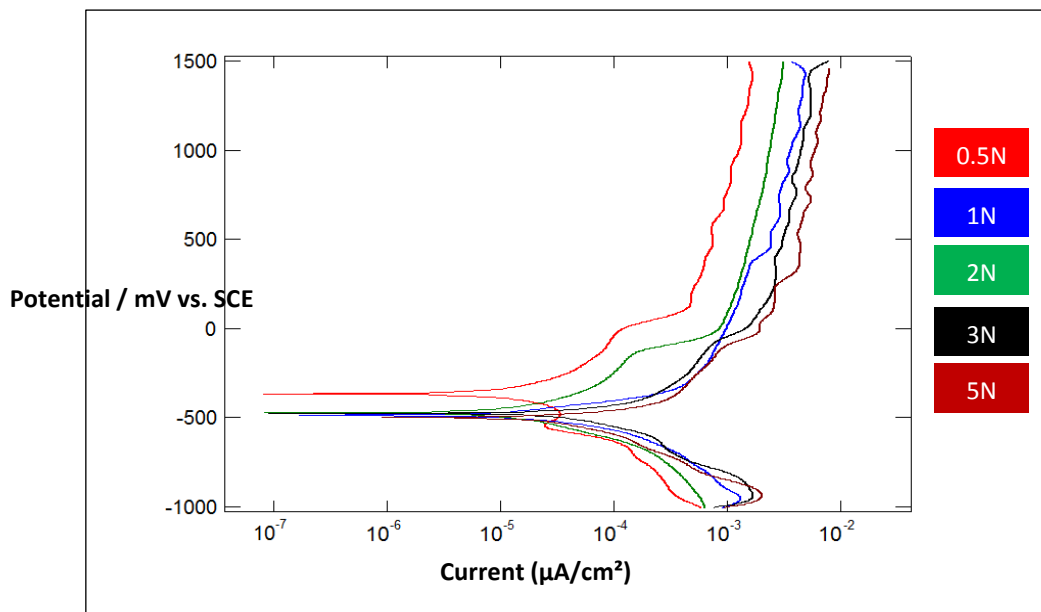
Polarisation sweeps were also performed to observe the change in electrochemical behaviour in the presence of additional SiC particles (Fig. 5b). The range of E_{corr} generally remained similar to the results seen in the absence of particles, with increasing applied the E_{corr} shifts in the positive direction and is more prominent which indicates the mass loss due to corrosion may have been enhanced. In both test solutions, with and without particles a sudden negative shift can be seen under an applied load of 5N. This shift indicates that the corrosion was inhibited and may be load dependant. In the case of pure NaCl solution (Fig. 5c) the E_{corr} appears to remain the same for different applied loads unlike the latter conditions. In general there is good evidence to suggest that the presence of protein in the NaCl solution effects the electrochemical behaviour. With the addition of particles the corrosion behaviour appears to have been enhanced.



(a)



(b)

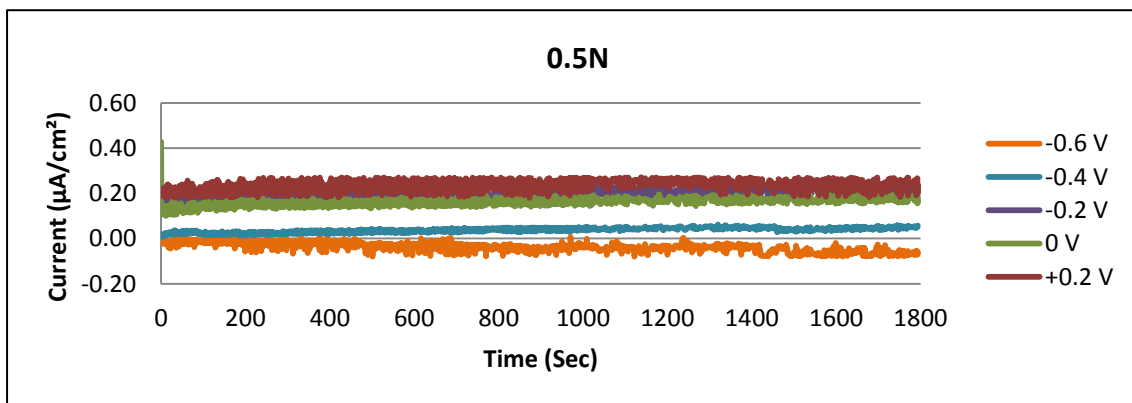


(c)

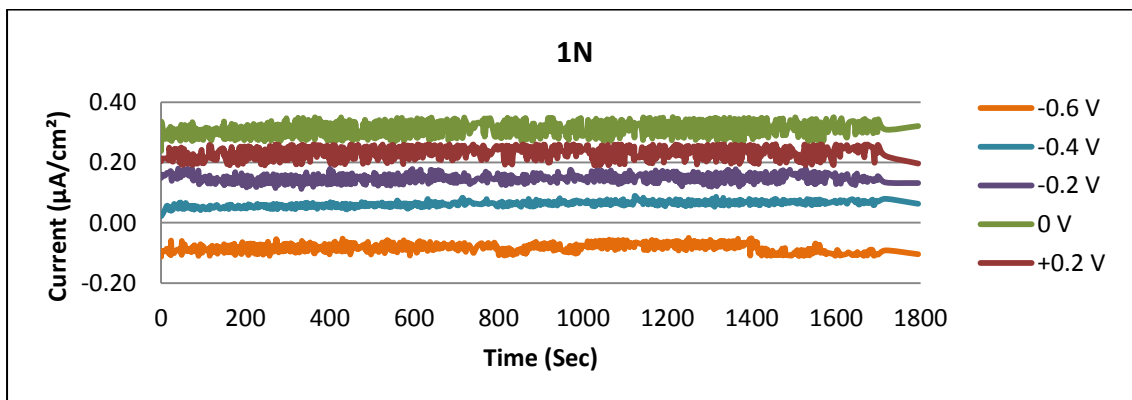
Figure 5: Polarisation curves for CoCrMo alloy for different applied loads in 0.9% NaCl (pH 7.3, 25°C) and : a) 10% FCS; b) 10% FCS and SiC particle (0.25 g cm^{-3}); c) pure NaCl solution

2.2. Potentiostatic measurements

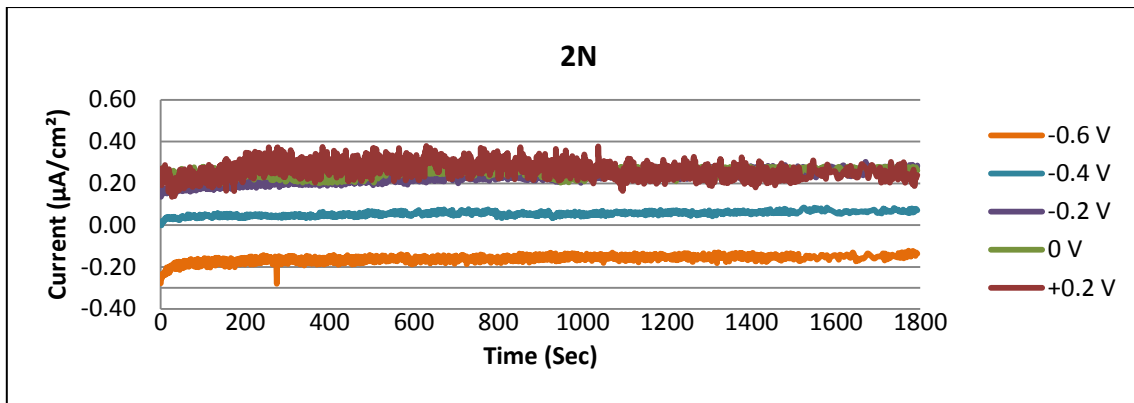
Potentiostatic measurements were carried out in order to evaluate the effect of potential and applied load on the corrosion behaviour. The results are shown graphically for the individual applied loads (Fig. 6) and applied potentials (Fig. 7). At the lower potentials the corrosion current is generally cathodic dominant. The measured current is most likely due to the reduction of water and dissolved oxygen. A general trend can be observed as the potential is increased; the measured current tends to increase anodically suggesting some enhancement of the passivation process. At the higher potentials investigated (0 and 200mV), the corrosion behaviour seem similar.



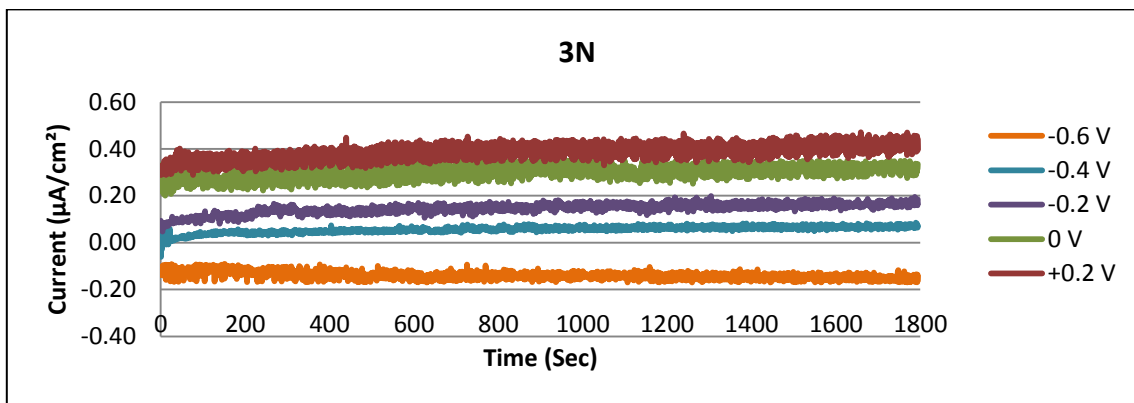
(a)



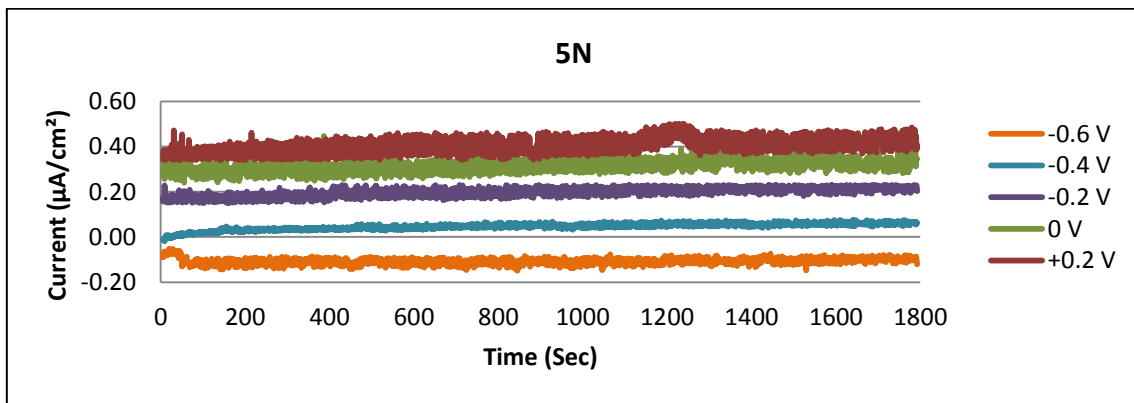
(b)



(c)

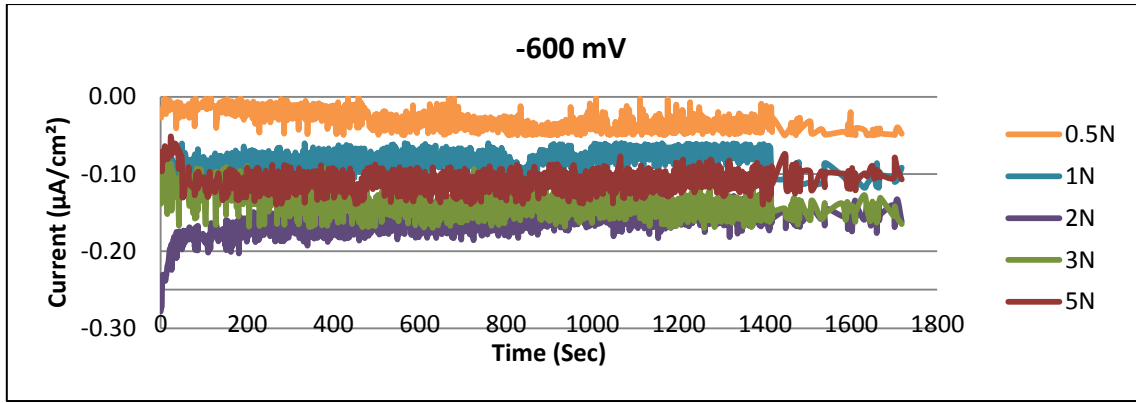


(d)

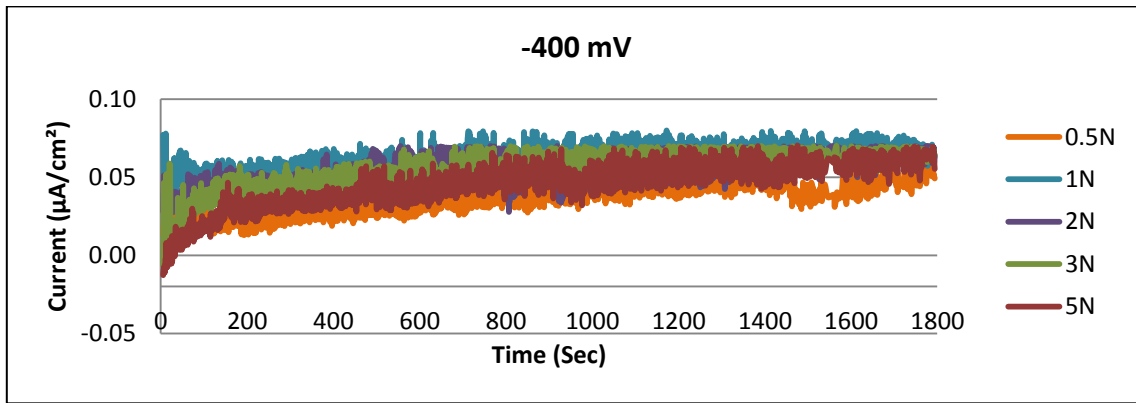


(e)

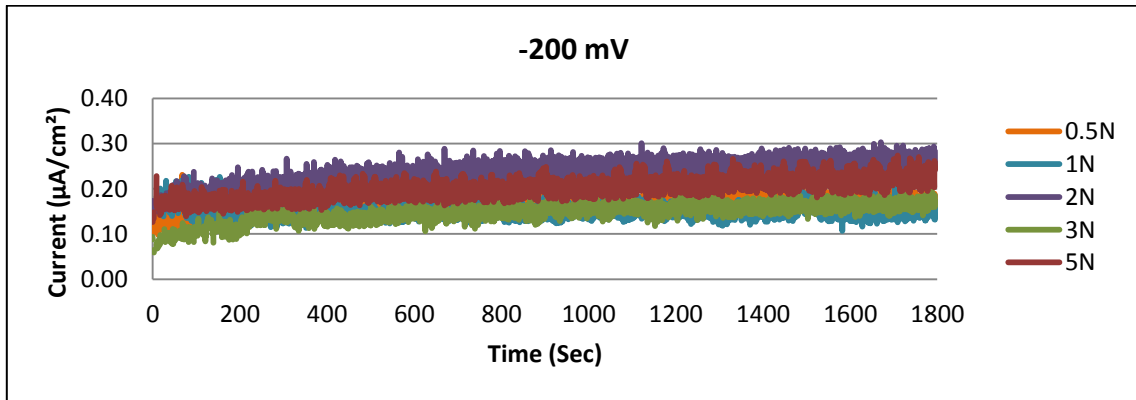
Figure 6: Potentiostatic current densities measured during micro-abrasion for various applied loads at different applied potentials in protein solution (pH 7.3, 25°C). From top a) 0.5N; b) 1N; c) 2N; d) 3N; e) 5N



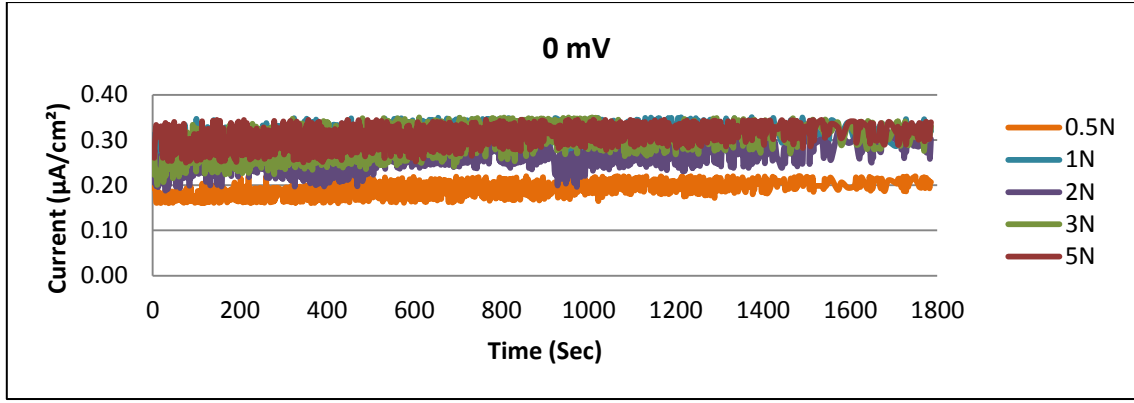
(a)



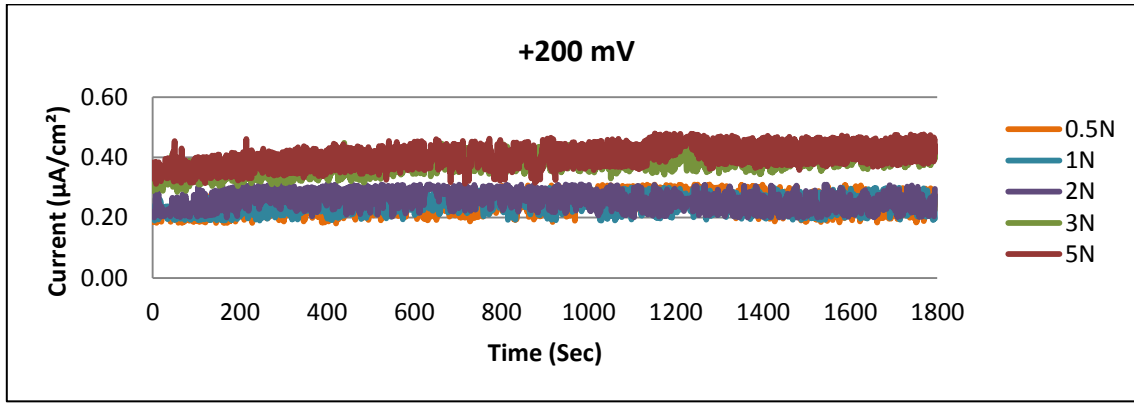
(b)



(c)



(d)



(e)

Figure 7: Potentiostatic current densities measured during micro-abrasion for various applied potentials at different applied loads in physiological solution (pH 7.3, 25°C). From top a) -600; b) -400; c) -200; d) 0; e) +200 mV

2.3. Mass loss data

The mass loss was determined according to an established method [15, 16], based on the analysis used to characterise the various components of the wear-corrosion process [17]:

$$\text{If: } K_{ac} = K_a + K_c \quad (2)$$

where, K_{ac} (g) is the total mass of material removed due to micro-abrasion-corrosion; K_a (g) the mass of material removed due to abrasion; and K_c (g) the total mass of material removed due to corrosion. The results are shown in Fig. 10.

$$K_a \text{ can be written as } K_a = K_{ao} + \Delta K_a \quad (3)$$

where K_{ao} is the mass loss due to micro-abrasion in the absence of corrosion; ΔK_a is the “synergistic” effect of corrosion on the abrasion, where the synergy component is a negative value it is then termed “antagonistic”.

$$K_c \text{ can be written as } K_c = K_{co} + \Delta K_c \quad (4)$$

where K_{co} is the mass loss due to corrosion in the absence of wear; ΔK_c is the enhanced mass loss of corrosion due to abrasion, also known as the “additive” effect.

Hence, the total micro-abrasion-corrosion rate can be given as follows:

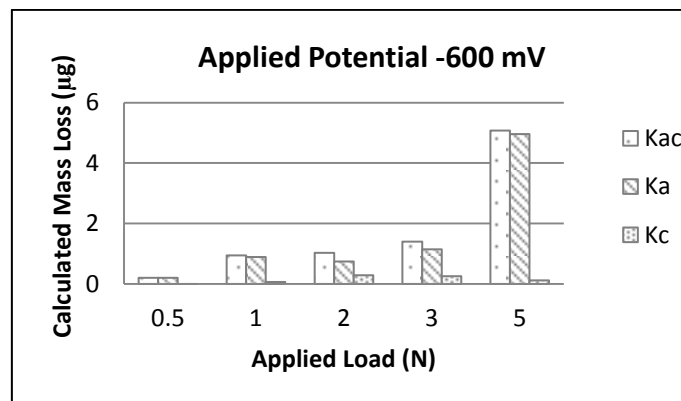
$$K_{ac} = K_{ao} + \Delta K_a + K_{co} + \Delta K_c \quad (5)$$

The corrosion mass losses K_c and K_{co} were derived using Faraday’s law i.e.,

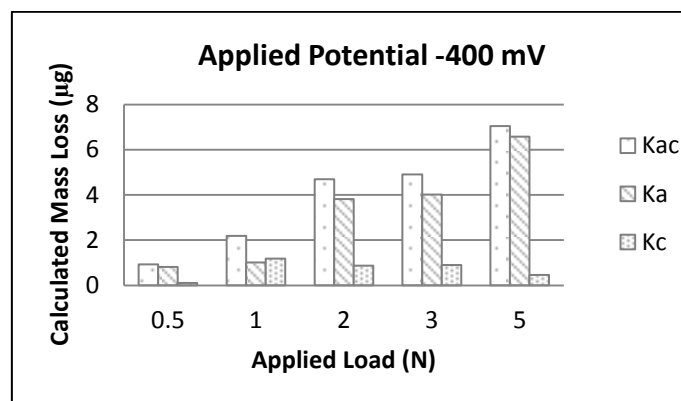
$$K_c = \frac{Q}{ZF} \quad (6)$$

$$K_{co} = \frac{M_w i t}{ZF} \quad (7)$$

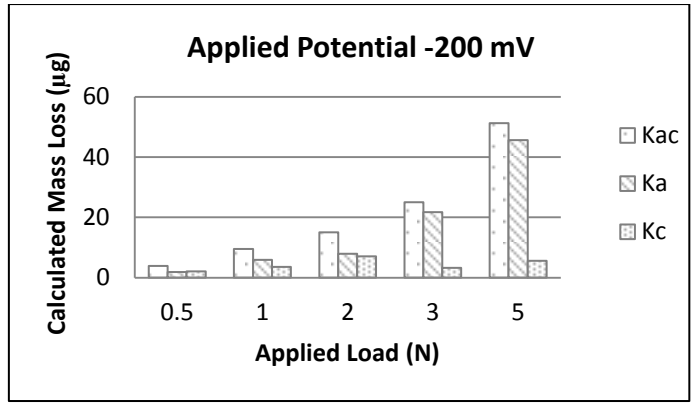
where Q is the charge passed (C); F is Faraday’s constant ($96,500 \text{ C mol}^{-1}$); z is the number of electrons involved in the corrosion process; i is the total current; t is the exposure time and M_w is the molar mass of the material (g mol^{-1}). The calculated mass loss due to wear in the absence of corrosion, K_{ao} , was estimated by abrasion-corrosion under testing cathodic conditions at an applied potential of -0.96 V.



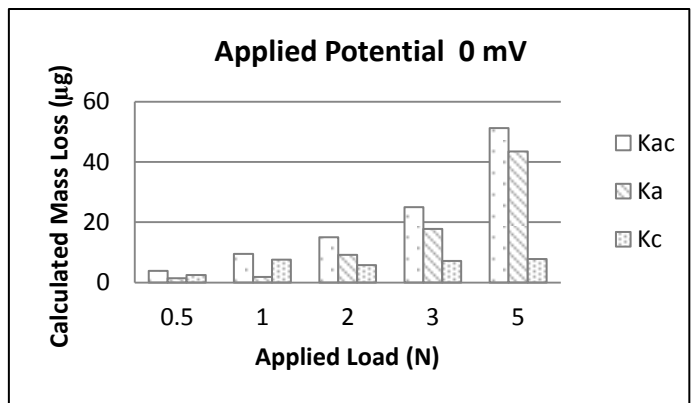
(a)



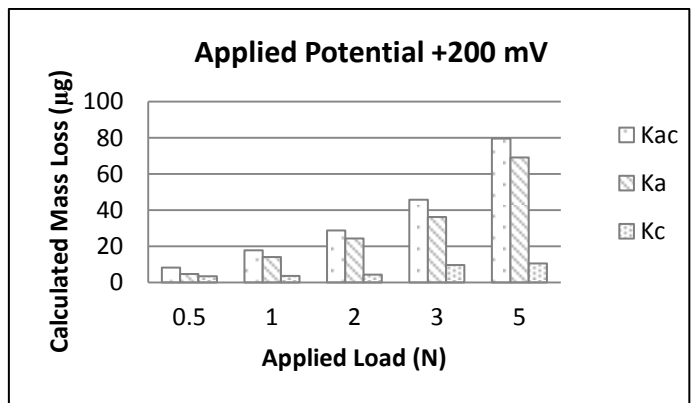
(b)



(c)



(d)



(e)

Figure 8: Calculated micro-abrasion-corrosion mass loss components for CoCrMo alloy in physiological solution (pH 7.3, 25°C). From top a) -600; b) -400; c) -200; d) 0; e) +200 mV

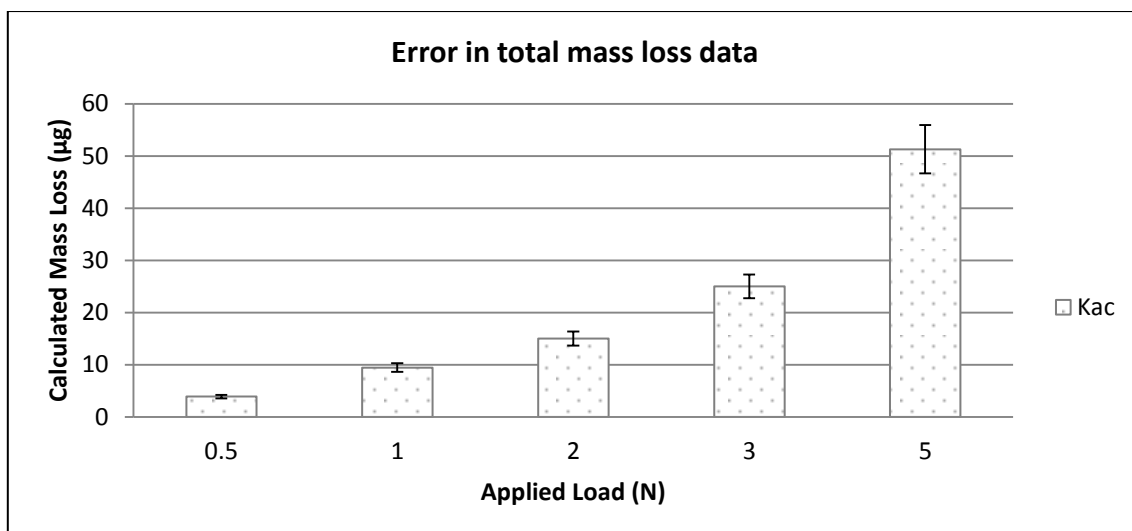


Figure 9: Variation in calculated total mass loss (K_{ac}) during 0 mV applied potential vs. increasing applied, experimental error shown for repeat readings ($n=3$) at each load and estimate to be $\pm 9\%$.

Table 3: K_c/K_a values at variable applied potential and loads

Applied Potential (mV/ SCE)	Applied Load (N)	K_{ac} (μg)	K_c (μg)	K_a (μg)	K_c/K_a
(a) -600	0.5	0.20	0.00	0.20	0.00
	1	0.95	0.06	0.89	0.07
	2	1.03	0.29	0.74	0.39
	3	1.40	0.25	1.15	0.22
	5	5.07	0.12	4.95	0.02
(b) -400	0.5	0.92	0.11	0.81	0.14
	1	2.19	1.18	1.01	1.17
	2	4.69	0.87	3.82	0.23
	3	4.91	0.90	4.01	0.22
	5	7.05	0.47	6.58	0.07
(c) -200	0.5	3.90	2.07	1.83	1.13
	1	9.46	3.53	5.93	0.60
	2	15.03	7.06	7.97	0.89
	3	25.02	3.28	21.74	0.15
	5	51.29	5.62	45.67	0.12
(d) 0	0.5	3.90	2.51	1.38	1.81
	1	9.46	7.59	1.87	4.06
	2	15.03	5.80	9.23	0.63
	3	25.02	7.19	17.83	0.40
	5	51.29	7.82	43.47	0.18
(e) +200	0.5	8.28	3.53	4.76	0.74
	1	17.75	3.67	14.07	0.26
	2	28.74	4.33	24.41	0.18
	3	45.84	9.72	36.12	0.27
	5	79.58	10.51	69.07	0.15

Table 4: $\Delta K_a / \Delta K_c$ values at variable applied potential and loads

Applied Potential (mV/ SCE)	Applied Load (N)	ΔK_a (μg)	ΔK_c (μg)	$\Delta K_a / \Delta K_c$	Wear Regime
(a) -600	0.5	0.00	0.00	0.01	Additive
	1	-0.06	0.06	-1.62	Antagonistic
	2	-0.29	0.29	-1.09	Antagonistic
	3	-0.25	0.25	-1.10	Antagonistic
	5	-0.12	0.12	-1.25	Antagonistic
(b) -400	0.5	0.61	0.11	6.91	Synergistic
	1	0.06	1.18	0.05	Additive
	2	2.79	0.87	3.28	Synergistic
	3	2.61	0.90	2.99	Synergistic
	5	1.51	0.47	3.41	Synergistic
(c) -200	0.5	1.63	2.07	0.79	Additive-synergistic
	1	4.98	3.53	1.42	Synergistic
	2	6.93	7.06	0.99	Additive-synergistic
	3	20.34	3.28	6.25	Synergistic
	5	40.60	5.62	7.26	Synergistic
(d) 0	0.5	1.18	2.51	0.48	Additive-synergistic
	1	0.92	7.59	0.12	Additive-synergistic
	2	8.19	5.80	1.42	Synergistic
	3	16.44	7.19	2.29	Synergistic
	5	38.40	7.82	4.93	Synergistic
(e) +200	0.5	4.56	3.53	1.30	Synergistic
	1	13.13	3.67	3.60	Synergistic
	2	23.37	4.33	5.43	Synergistic
	3	34.72	9.72	3.58	Synergistic
	5	64.00	10.51	6.10	Synergistic

4. Discussion

4.1. Significance of trends in polarisation data, mass loss data and micrographs

Polarisation sweeps (Fig. 5) showed similar trends during micro-abrasion-corrosion in the presence of FCS solution both with and without additional particles. Similar to previous work conducted in Ringer's solution [15], the results indicated passivation behaviour between the range of -0.25 and +0.25 V in both presence and absence of particles in FCS solution. However in this study a slight but more prominent shift of E_{corr} was observed with the addition, but not in the absence of particles. The presence of protein may play a significant role during particle interaction at the surface contact and enhancing the corrosion behaviour, which has been shown in several other studies [18, 19]. Interestingly, the results of the experiments conducted in the present study indicate that, at the highest applied load of 5N, the E_{corr} and I_{corr} value shifted cathodically and was much lower than that observed at the lowest applied load 0.5N. It follows that although there may be some trend as the applied load is increased at the lower loads, it may only occur during a narrow range of loads where at higher loads a significant wear transition occurs.

Potentiostatic tests further indicated a significant transition in measured currents at variable applied potentials (Figs. 6 and 7). For the range of applied loads tested, corrosion was shown to increase with increased potential suggesting load dependant corrosion behaviour i.e. increased mass loss towards from cathodic to anodic potentials. At applied potentials above -0.2V the current is shown to increase only slightly when compared to the lower values. This is in agreement with the polarisation sweep behaviour where it is thought passivation occurs between -0.25 and +0.25V. When the total mass losses are considered (Fig. 8), it can be seen clearly that mass loss due to corrosion plays a lesser role and remains very much independent for the range of applied loads. The mass loss due to abrasion is significantly more dominant throughout and this behaviour is very much identical at all applied loads. This should be expected since CoCr alloy is a highly corrosion resistant material due to the known formation of a chromium oxide layer which inhibits corrosion activity. Additionally the total mass loss tends to increase with increasing applied load. This is in good agreement with the Archard wear model [20].

It is therefore reasonable to assume the dominant mechanism underlying the material mass loss may be due to abrasion. This can be confirmed based on the wear scar analysis on SEM (Fig. 3) and AFM (Fig. 4), where there is clear indication of 2-body abrasion from the parallel and uniform grooved pattern on the wear scar surface. However, in other tribocorrosion related work [8] it is well established that the total mass loss is not simply the summation of corrosion wear and mechanical wear losses. There is a synergistic component as was shown by Mathew et al. for a similar study investigating the effects of protein (FCS) on CoCr [18]. The study quantified the individual mass loss contributions and showed that around 1/3 of the mass loss was due to a synergistic effect, where pure wear dominated and pure corrosion played only a minor role in the total mass loss. In the same study however, it was not shown how the synergy effect may transition over a window of parameters.

4.2. Wastage maps

A wastage map (Fig. 10a) has been constructed based on the results for overall weight loss (K_{ac}) as a function of applied potentials and applied loads. The boundaries defining wastage regime from previous work [15] have been used in the map construction so that comparisons may be made. The maximum hip contact pressures corresponding to the applied loads were determined using Hertzian formulae for ball/ flat contact [21] and varied between 9.6 and 20.6 MPa corresponding to the applied loading range. Computational simulation studies of the Charnley hip have indicated a maximum hip contact pressure around ~ 18 MPa [22]. In hip joint simulations of CoCr alloy the average calculated pressure was found to range between 14 and 60 MPa [8]. More recently, it has been shown during micro-lateralization contact pressures can reach up to 900 MPa at the acetabular bearing surface in metal-on-metal hip implant for a spherical contact, this remained at around 230 MPa in a non-spherical contact [23].

The wastage regime boundaries in the current study are as follows:

$$K_{ac} \leq 3 \times 10^{-6}g \quad (\text{low}) \quad (8)$$

$$3 \times 10^{-6}g < K_{ac} \leq 6 \times 10^{-6}g \quad (\text{medium}) \quad (9)$$

$$K_{ac} > 6 \times 10^{-6}g \quad (\text{high}) \quad (10)$$

The wastage map indicates a clear transition in overall wastage rate. For loads less than 1N an expected low wastage regime dominates over the range of applied potentials investigated. Over the cathodic range of potentials, the wastage regimes remains low despite increasing load, towards the higher load a transition to medium wastage is observed. In comparison to an earlier study [17] there is some similarity where a medium wastage regime dominated for the most part under the same conditions. The main difference between both is that in this study a high wastage regime dominates for increasing loads higher than 1N above cathodic potentials. The presence of protein in the solution may enhance low-medium wastage at low loads and potentials, but beyond this range at increased loads it appears that the solution may have accelerated wastage when compared to the previous study which used Ringer's solution. The map demonstrates the wastage regime is consistently low-medium at lower loads and transitions to high wastage rates with increased load and potential.

4.3. Micro-abrasion-corrosion regime maps

Adachi and Hutchings [24] developed the theoretical model to describe the transitions in micro-abrasion, wear in the 1-5N load range can be described as 2 body grooving. This is consistent for the current work as can be observed by the wear patterns generated the loading range stated (Fig. 3 and 4). It is also necessary to mention based on the work of Adachi and Hutchings, at loads less than 1N a transition occurs from rolling to grooving. The micro-abrasion-corrosion map was developed on this basis and follows from similar maps

developed for steel/polymer couple in aqueous conditions [16]. The ratio of the micro-abrasion to corrosion contribution defines the dominant wear mechanism as follows:

$$\frac{K_c}{K_a} \leq 0.1 \quad (\text{micro-abrasion dominated}) \quad (11)$$

$$0.1 < \frac{K_c}{K_a} \leq 1 \quad (\text{micro-abrasion- passivation}) \quad (12)$$

$$1 < \frac{K_c}{K_a} \leq 10 \quad (\text{passivation- micro-abrasion}) \quad (13)$$

$$\frac{K_c}{K_a} > 10 \quad (\text{passivation- dominated}) \quad (14)$$

Previous efforts have also involved attempts to describe the sub-division mechanisms of those defined above [16]; the method established is by inspection of the polarization data and identifying the state of corrosion as either active or passive. The mechanistic map obtaining from this work is shown in Fig. 10(b). At cathodic potentials pure micro-abrasion is the dominant wear mechanism, which is consistent with the polarization data indicating corrosion does not occur. As the potential is increased to more anodic values micro-abrasion remains dominant at the higher loads, which then transitions to a mixed regime as the load drops below 3N in which micro-abrasion-passivation dominates. This is also consistent with the earlier study on CoCrMo in Ringer's solution [15] where micro-abrasion-passivation was found to be the dominant mechanism above cathodic potentials. In this study, however, there is a definite transition to a passivation-micro-abrasion regime at the lower loads above cathodic potential. This was not observed in previous work, which may be due to the presence of protein lubricating the surface, consistent with the model developed by Adachi and Hutching. In several of the previous studies [15, 16] a peak was observed at around 0V in steel/ polymer and also CoCrMo/UHMWPE couplings and in this study a similar peak can also be observed at 0V; this would suggest that the passivation-micro-abrasion regime is prolonged with increasing load due to the applied potential. The presence of protein in solution may have enhanced this regime demonstrating a protective mechanism during the potential range studied.

Furthermore it is useful to study the synergistic effects of the tribocorrosion process. The regimes are based on the those developed by Stack et al. for erosion-corrosion studies [25]. The ratios are taken from the 'synergistic' effect of corrosion on the wear rate ΔK_a , and the enhancement of corrosion due to micro-abrasion ΔK_c or 'additive' effect. Where the values are shown as negative it is considered antagonistic effects; here the actions of micro-abrasion and corrosion neither enhance nor synergise one another. The regimes may be defined as follows:

$$\frac{\Delta K_a}{\Delta K_c} \leq 0.1 \quad (\text{additive}) \quad (15)$$

$$0.1 < \frac{\Delta K_a}{\Delta K_c} \leq 1 \quad (\text{additive-synergistic}) \quad (16)$$

$$\frac{\Delta K_a}{\Delta K_c} > 1 \quad (\text{synergistic}) \quad (17)$$

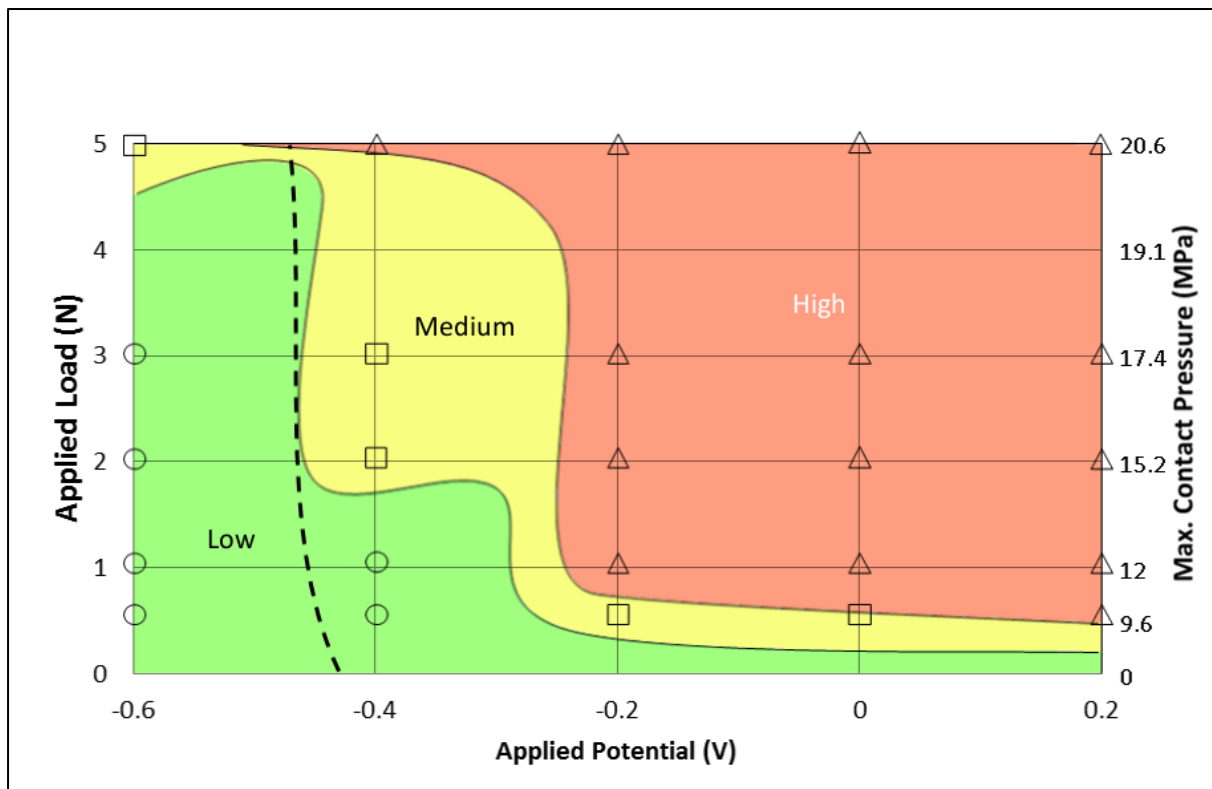
The synergy map developed from this study shown in Fig. 10(c) shows, for the parameters tested, a synergistic regime dominates above cathodic potentials. There is a clear transition to an additive-synergistic regime over the same potential range for lower loads. Unlike in the earlier work [16] where testing was conducted in Ringer's solution, its corresponding map indicated a dominant antagonistic regime. This can be observed for a small range in the current result at close to cathodic potential only. Considering the differences in replacing the solution from a non-protein to a protein-based solution, it is reasonable to suggest that the presence of protein does effect the transitioning in wear behaviour. In other similar work, Sun et al., [10] showed that the protein adsorption (bovine serum) on CoCrMo alloy in a similar setup reduced wear rates during sliding wear corrosion. During sliding at lower loads in the current work, a low-medium wastage rate regime dominated. Also the concentration of protein in this study was kept at 10% volume, so it is not clear what the effect will be for different concentrations of protein solution for the same conditions. Sun et al. also showed for the same conditions. In the presence of particles the protein appeared to accelerate the wear due to increased particle entrainment, it is likely particle aggregation occurred at the surface contact.

In addition to the oxide film formation on the metal surface which is well established [26], there is formation of a tribological film on the implant surface in hip replacement during tribocorrosion [6, 8], and it is known to provide protective mechanisms under optimal conditions. It has been shown that the film is composed of denatured protein originating from the fluid surrounding the hip replacement. Studies have shown the tribofilm may provide a beneficial barrier to corrosion and also lubrication to facilitate sliding. It may explain the results of this study and suggests a mechanistic tribo-corrosion process as follows:

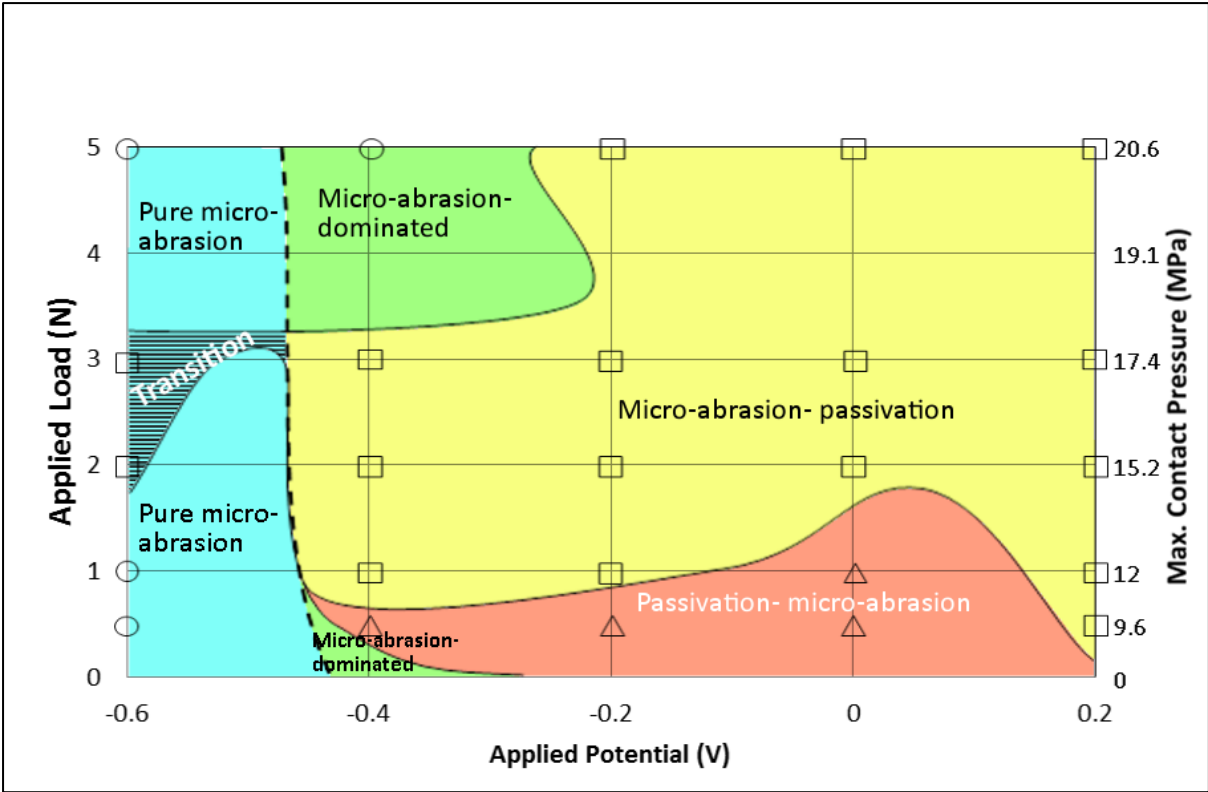
- (i) A tribological film composed of denatured protein may form on the contact surface where at lower loads, can be observed as passivation-micro-abrasion and low-medium wastage regimes; and
- (ii) At increased loading and over a range of applied voltage potentials the tribofilm may breakdown or become inhibited due to the operating conditions of this study.

There are many questions that remain to be addressed, however, there is a need for further detailed investigations to fully establish the wear mechanisms from the micro-abrasion-corrosion perspective. Moreover, it is not certain at this stage whether in fact a tribofilm did form during the conditions of this study. It is likely under *in-vivo* conditions, however, that a tribofilm exists at the implant surface and provides a number of protective benefits against tribocorrosion. In a recent study investigating protein film formation in artificial joints Myant et al. [27] showed under repeated loading a thin solid film (~4nm) formed on the implant contact surfaces when operating in a protein solution, which may act as a lubricant. In a related work this was also shown in the work of Yan et al. [19] where tribocorrosion testing was conducted for CoCrMo in 50% bovine serum, the corrosion was inhibited during sliding wear. In the present study a concentration of 10% serum was used, and the presence

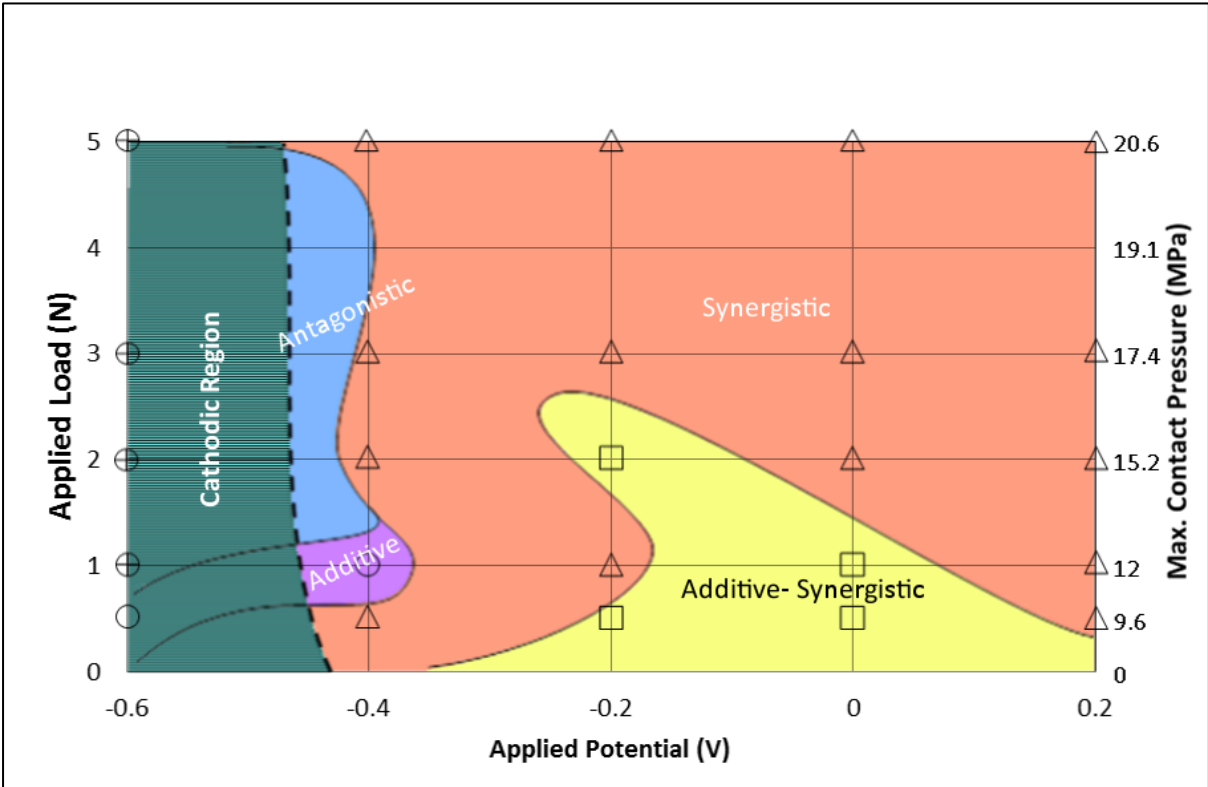
of protein in the solution may have formed a protective layer as described in other studies. The mechanism map indicates at the lower load this may be the case where a passivation-micro-abrasion regime dominates which is also reflected in the wastage map. With increasing load above 1N however there is a transition to micro-abrasion-passivation regime, which may be due to the removal of the protein film under the action of the abrasion with increased load at a concentration of 10% serum. Further wear maps need to be constructed for increasing protein concentrations in order to completely assess the transitioning behaviours due to protein. It is important to note that the objective of the work was to demonstrate the concept of micro-abrasion-corrosion mapping for a clinical application. In this study the hip contact conditions are simplified, for future work the wear maps will be developed on more realistic and biomechanically accurate hip simulations.



(a)



(b)



(c)

Figure 10: Micro-abrasion-corrosion regime maps for CoCrMo alloy in physiological solution (pH 7.3, 25°C): a) wastage map; b) mechanism map; c) synergy map

5. Conclusions

(i) In this study the effects of applied potential and applied loads were investigated for CoCrMo in a physiological solution.

(ii) The construction of wear maps was also demonstrated which showed the micro-abrasion-corrosion transitions of CoCrMo in the presence of protein.

(ii) The presence of a denatured protein film inhibited wear at lower loads while accelerating it at higher values.

(iii) As part of progressive understanding of the wear behaviour of such implant material the interaction of proteins and surface oxide/ protein layer will be investigated using surface analysis techniques including AFM and SEM.

(iv) The results indicated that proteins present in foetal calf serum solution may play a critical role in enhancing or protecting against tribo-corrosive degradation.

Acknowledgements

The authors wish to acknowledge the UK Engineering & Physical Sciences Research Council (EPSRC) Doctoral Training Centre in Medical Devices, University of Strathclyde (EPSRC Grant Ref. EP/F50036X/1) for sponsorship of this work. We are also grateful to Dr. Mathew T. Mathew (Rush Medical University, Chicago) for kindly donating the supply of CoCrMo alloy.

References

- [1] M.M. Stack, Mapping tribo-corrosion processes in dry and in aqueous conditions: some new directions for the new millennium, *Tribology International*, 35 (2002) 681-689.
- [2] M.M. Stack, Bridging the gap between tribology and corrosion: from wear maps to Pourbaix diagrams, *Int Mater Rev*, 50 (2005) 1-17.
- [3] S.C. Lim, M.F. Ashby, Wear-Mechanism maps, *Acta Metallurgica*, 35 (1987) 1-24.
- [4] D. Landolt, S. Mischler, M. Stemp, Electrochemical methods in tribocorrosion: a critical appraisal, *Electrochimica Acta*, 46 (2001) 3913-3929.
- [5] M.T. Mathew, P. Srinivasa Pai, R. Pourzal, A. Fischer, M.A. Wimmer, Significance of Tribocorrosion in Biomedical Applications: Overview and Current Status, *Advances in Tribology*, 2009 (2009).
- [6] Y. Liao, E. Hoffman, M. Wimmer, A. Fischer, J. Jacobs, L. Marks, CoCrMo metal-on-metal hip replacements, *Physical Chemistry Chemical Physics*, 15 (2013) 746-756.
- [7] A. Buford, T. Goswami, Review of wear mechanisms in hip implants: Paper I – General, *Materials & Design*, 25 (2004) 385-393.
- [8] S. Mischler, A.I. Muñoz, Wear of CoCrMo alloys used in metal-on-metal hip joints: A tribocorrosion appraisal, *Wear*, 297 (2013) 1081-1094.
- [9] A.J. Gant, M.G. Gee, A review of micro-scale abrasion testing, *Journal of Physics D: Applied Physics*, 44 (2011) 073001.
- [10] D. Sun, J.A. Wharton, R.J.W. Wood, The effects of proteins and pH on tribo-corrosion performance of cast CoCrMo: a combined electrochemical and tribological study, *Tribology – Materials, Surfaces & Interfaces*, 2 (2008) 150-160.
- [11] D. Sun, J.A. Wharton, R.J.K. Wood, Abrasive size and concentration effects on the tribo-corrosion of cast CoCrMo alloy in simulated body fluids, *Tribology International*, 42 (2009) 1595-1604.
- [12] D. Sun, J.A. Wharton, R.J.K. Wood, L. Ma, W.M. Rainforth, Microabrasion–corrosion of cast CoCrMo alloy in simulated body fluids, *Tribology International*, 42 (2009) 99-110.
- [13] D. Sun, J.A. Wharton, R.J.K. Wood, Micro- and Nano-scale Tribo-Corrosion of Cast CoCrMo, *Tribol Lett*, 41 (2011) 525-533.
- [14] M.A. Wimmer, A. Fischer, R. Buscher, R. Pourzal, C. Sprecher, R. Hauert, J.J. Jacobs, Wear mechanisms in metal-on-metal bearings: the importance of tribochemical reaction layers, *J Orthop Res*, 28 (2010) 436-443.
- [15] M.M. Stack, J. Rodling, M.T. Mathew, H. Jawan, W. Huang, G. Park, C. Hodge, Micro-abrasion–corrosion of a Co–Cr/UHMWPE couple in Ringer's solution: An approach to construction of mechanism and synergism maps for application to bio-implants, *Wear*, 269 (2010) 376-382.
- [16] M.M. Stack, H. Jawan, M.T. Mathew, On the construction of micro-abrasion maps for a steel/polymer couple in corrosive environments, *Tribology International*, 38 (2005) 848-856.
- [17] Z. Yue, P. Zhou, J. Shi, Some factors influencing erosion-corrosion performance of materials, in: K.C. Ludema (Ed.) *Proceedings of the Conference on Wear of Materials*, ASME, 1987, pp. 763.
- [18] M.T. Mathew, J.J. Jacobs, M.A. Wimmer, Wear-corrosion synergism in a CoCrMo hip bearing alloy is influenced by proteins, *Clinical orthopaedics and related research*, 470 (2012) 3109-3117.
- [19] Y. Yan, A. Neville, D. Dowson, Biotribocorrosion of CoCrMo orthopaedic implant materials—Assessing the formation and effect of the biofilm, *Tribology International*, 40 (2007) 1492-1499.
- [20] J.F. Archard, Contact and rubbing of flat surfaces, *Journal of Applied Physics*, 24 (1953) 981.

- [21] G. Stachowiak, A.W. Batchelor, Engineering Tribology, Butterworth-Heinemann, 2011.
- [22] X. Hua, B.M. Wroblewski, Z. Jin, L. Wang, The effect of cup inclination and wear on the contact mechanics and cement fixation for ultra high molecular weight polyethylene total hip replacements, *Medical Engineering & Physics*, 34 (2012) 318-325.
- [23] L. Wang, X. Liu, D. Li, F. Liu, Z. Jin, Contact mechanics studies of an ellipsoidal contact bearing surface of metal-on-metal hip prostheses under micro-lateralization, *Medical Engineering & Physics*, 36 (2014) 419-424.
- [24] K. Adachi, I.M. Hutchings, Wear-mode mapping for the micro-scale abrasion test, *Wear*, 255 (2003) 23-29.
- [25] M.M. Stack, T.M. Abd El Badia, On the construction of erosion–corrosion maps for WC/Co–Cr-based coatings in aqueous conditions, *Wear*, 261 (2006) 1181-1190.
- [26] A.W.E. Hodgson, S. Kurz, S. Virtanen, V. Fervel, C.O.A. Olsson, S. Mischler, Passive and transpassive behaviour of CoCrMo in simulated biological solutions, *Electrochimica Acta*, 49 (2004) 2167-2178.
- [27] C. Myant, R. Underwood, J. Fan, P.M. Cann, Lubrication of metal-on-metal hip joints: The effect of protein content and load on film formation and wear, *Journal of the Mechanical Behavior of Biomedical Materials*, 6 (2012) 30-40.

List of figure captions

Figure 1: Micro-abrasion-corrosion test apparatus.....	6
Figure 2: Micro-abrasion-corrosion testing procedure for CoCrMo alloy in physiological solution	7
Figure 3: SEM scans showing wear scars for CoCrMo generated at an applied load of 5N during +200 mV applied potential: a) scar diameter; b) parallel grooves with embedded particles on crater surface.	8
Figure 4: AFM scans of wear scar surface for an applied load of 5N vs. applied potential +200 mV: a) distinct parallel grooves across the surface indicating a 2-body abrasion regime, small particles appear to be embedded at the surface; b) 3D scan image for the scar surface indicates the depth of the abraded grooves.	9
Figure 5: Polarisation curves for CoCrMo alloy for different applied loads in 0.9% NaCl (pH 7.3, 25°C) and : a) 10% FCS; b) 10% FCS and SiC particle (0.25 g cm^{-3}); c) pure NaCl solution	11
Figure 6: Potentiostatic current densities measured during micro-abrasion for various applied loads at different applied potentials in protein solution (pH 7.3, 25°C). From top a) 0.5N; b) 1N; c) 2N; d) 3N; e) 5N	13
Figure 7: Potentiostatic current densities measured during micro-abrasion for various applied potentials at different applied loads in physiological solution (pH 7.3, 25°C). From top a) -600; b) -400; c) -200; d) 0; e) +200 mV	15
Figure 8: Micro-abrasion-corrosion mass loss components for CoCrMo alloy in physiological solution (pH 7.3, 25°C). From top a) -600; b) -400; c) -200; d) 0; e) +200 mV.....	17
Figure 9: Variation in total mass loss (K_{ac}) during 0 mV applied potential vs. increasing applied, experimental error shown for repeat readings (n=3) at each load and estimate to be $\pm 9\%$	18
Figure 10: Micro-abrasion-corrosion regime maps for CoCrMo alloy in physiological solution (pH 7.3, 25°C): a) wastage map; b) mechanism map; c) synergy map	25

List of table captions

Table 1: Chemical composition of CoCrMo	5
Table 2: Material properties	5
Table 3: K_c/K_a values at variable applied potential and loads	18
Table 4: $\Delta K_a/\Delta K_c$ values at variable applied potential and loads	19